

Article

Synergistic Integration of MXene and Metal-Organic Frameworks for Enhanced Electrocatalytic Hydrogen Evolution in an Alkaline Environment

Low Ping Hao ¹, Abdul Hanan ², Rashmi Walvekar ^{1,*}, Mohammad Khalid ^{2,3,4,*}, Faiza Bibi ², Wai Yin Wong ⁵ and Chander Prakash ⁶

¹ School of New Energy and Chemical Engineering, Xiamen University Malaysia, Jalan Sunsuria, Bandar Sunsuria, Sepang 43900, Selangor, Malaysia; cme1904905@xmu.edu.my

² Graphene & Advanced 2D Materials Research Group (GAMRG), School of Engineering and Technology, Sunway University, No. 5, Jalan Universiti, Bandar Sunway, Petaling Jaya 47500, Selangor, Malaysia; ahanansamo@gmail.com (A.H.); faiza.b@mail.sunway.edu.my (F.B.)

³ Division of Research and Development, Lovely Professional University, Phagwara 144411, Punjab, India

⁴ School of Applied and Life Sciences, Uttarakhand University, Dehradun 248007, Uttarakhand, India

⁵ Fuel Cell Institute, Universiti Kebangsaan Malaysia, Bangi UKM 43600, Selangor, Malaysia; waiyin.wong@ukm.edu.my

⁶ School of Mechanical Engineering, Lovely Professional University, Phagwara 144411, Punjab, India; chander.mechengg@gmail.com

* Correspondence: rashmi.walvekar@xmu.edu.my (R.W.); khalids@sunway.edu.my (M.K.)



Citation: Hao, L.P.; Hanan, A.; Walvekar, R.; Khalid, M.; Bibi, F.; Wong, W.Y.; Prakash, C. Synergistic Integration of MXene and Metal-Organic Frameworks for Enhanced Electrocatalytic Hydrogen Evolution in an Alkaline Environment. *Catalysts* **2023**, *13*, 802. <https://doi.org/10.3390/catal13050802>

Academic Editor: Jinsoo Kim

Received: 6 April 2023

Revised: 21 April 2023

Accepted: 23 April 2023

Published: 26 April 2023



Copyright: © 2023 by the authors. Licensee MDPI, Basel, Switzerland. This article is an open access article distributed under the terms and conditions of the Creative Commons Attribution (CC BY) license (<https://creativecommons.org/licenses/by/4.0/>).

Abstract: The development of transition metal (TM) catalysts to replace precious metals has garnered increasing interest. Specifically, platinum (Pt)-based catalysts have been extensively investigated for their electrochemical performance in hydrogen evolution reaction (HER), which offer a clean means of producing hydrogen fuel without carbon emissions. However, the reliance on Pt-based catalysts has hindered the progress of HER development. Therefore, researchers have explored metal-organic frameworks (MOFs) as a substitute for noble Pt-based catalysts to address this issue. Nevertheless, the low electroconductivity of pure MOFs restricts their application in electrochemical fields. To overcome this limitation, MXenes have emerged as a promising two-dimensional (2D) material for coupling with MOFs to create an electrocatalyst with high electrical conductivity, a large surface area, and a tunable structure. In this study, we report the synthesis of a $Ti_3C_2T_x$ (MXene) nanosheet-encapsulated MOFs catalyst ($Ti_3C_2T_x@ZIF-8$) with high activity and a low cost by encapsulating the precursor with ZIF-8 for HER in alkaline media. The catalyst exhibits an overpotential of only 507 mV at 20 mA/cm² and a low Tafel slope value of 77 mV/dec. Additionally, cyclic voltammetry (CV) indicates an electrochemical active surface area (ECSA) of 122.5 cm², and chronopotentiometry demonstrates the stable nature of the catalyst over 20 h without any significant changes in the overpotential value. The excellent electrochemical properties of $Ti_3C_2T_x@ZIF-8$ suggest its potential as a promising material for energy conversion applications.

Keywords: MXene; $Ti_3C_2T_x$; MOF; water splitting; electrocatalyst; HER

1. Introduction

There has been a surge of interest in the hydrogen evolution reaction (HER) due to the escalating demand for sustainable energy sources and the possibility of employing fuel cells as an eco-friendly technology. The electrochemical process of splitting water to generate hydrogen is a promising means of producing environmentally sustainable energy. However, an alternative approach to hydrogen production involves steam methane reforming (SMR) combined with water–gas shift (WGS) [1] and coal gasification. While these methods can generate larger quantities of hydrogen, they also result in negative environmental impacts, such as carbon dioxide emissions. In contrast, water electrolysis is an ecologically beneficial

method for long-term hydrogen production. Unfortunately, the oxygen evolution reaction (OER) associated with the hydrogen evolution reaction (HER) during water splitting is hindered by poor kinetics, making it a significant challenge [2–4]. Adding an efficient catalyst to stimulate these reactions is the most feasible way to overcome this problem. Due to their significant capacity to promote hydrogen (H_2) generation in water splitting, Pd- and Pt-based noble metals have been widely used as catalysts for electrochemical HER [5,6]. Whereas Pt-based catalysts perform well in HER, with a reference overpotential value near zero as well as a low Tafel slope value of around 30 mV/dec, the availability of this precious metal catalyst has hindered its use in larger-scale H_2 generation due to its high cost [7–12]. Metal-organic frameworks (MOFs), which consist of metal and organic ligands, can exist in both two-dimensional (2D) and three-dimensional (3D) forms. These materials have been extensively studied for their potential in electrocatalytic applications, particularly for oxygen evolution reaction (OER) and hydrogen evolution reaction (HER). The inorganic domains in MOFs, including layers, clusters, and chains, are connected to organic linkers and form 3D mixed frameworks through strong bonding and complex fractions. These 3D mixed frameworks exhibit exceptional electrocatalytic performance [13,14]. Zeolithic imidazolate frameworks (ZIFs) are a subclass of MOFs that are composed of imidazolate ligands coordinated with divalent metal cations (Zn^{2+} or Co^{2+}) [15]. The metal-imidazole-metal (M-Im-M) structure formed by the transition metal ion as well as the organic ligand in ZIFs has the same angle (145°) as the Si-O-Si link in conventional silica-based zeolites. ZIFs' distinct structure enables them to demonstrate improved stability and tunability, in addition to inheriting benefits such as the high specific surface and porosity of MOFs catalysis.

MXene, a two-dimensional material, possesses high electroconductivity, a tunable band structure, and hydrophilic properties [16,17]. Due to the strong covalent bonds and high atomic thickness of MXenes, they exhibit exceptional mechanical properties and flexibility, in addition to a high surface area-to-volume ratio [18,19]. Recently, MXene has been investigated for its potential as a catalyst for electrochemical applications. Wu et al. [20] reported the successful encapsulation of a 2D nanosheet morphology MOF (H_2TCPP) in V_2CT_x MXene, which resulted in a composite catalyst (V_2CT_xPMOF) with excellent electrocatalytic properties. The study found that MXene's highly electronegative terminating atoms and large surfaces enable the topological synthesis and growth of MOFs with a 2D morphology [20]. Additionally, MXene's hydrophilic properties make it suitable for water-splitting applications. Zong et al. [21] successfully synthesized a bi-functional catalyst ($Ti_2NT_x@ZIF-CoP$) by encasing an ultra-thin titanium-based MXene in a CoP composite produced from a MOF. The synthesized catalyst exhibited remarkable reaction kinetics, as evidenced by its low Tafel slope of 79.1 mV/dec and low overpotential of 112 mV in an alkaline setting. These findings highlight the potential of MXene-encased MOFs as efficient and versatile catalysts for electrochemical reactions.

Herein, we report the combination of MXenes ($Ti_3C_2T_x$) and ZIF-8 as a composite material for enhancing the HER performance. The combination of these materials results in a novel composite electrocatalyst with high electrical conductivity and a large number of active sites. The addition of ZIF-8 to the $Ti_3C_2T_x$ catalyst provides a stable and porous support structure, which further improves the HER performance in alkaline media. The synthesized material was characterized using various analytical techniques, including XRD, SEM, EDS, HRTEM, XPS, TGA, and FTIR, to determine its crystallinity, morphology, and elemental composition.

2. Results and Discussion

2.1. Characterizations

The X-ray diffraction (XRD) patterns of ZIF-8 ($C_{24}H_{30}N_{12}Zn_3$), $Ti_3C_2T_x$, and $Ti_3C_2T_x@ZIF-8$ are shown in Figure 1. The pure ZIF-8 characterization was verified at the first two 2θ peaks at 7.3° and 10.37° , 12.7° , 14.8° , 16.46° , and 18.1° , which are close to the simulated ZIF-8 peak values of 5° and 11° reported in earlier papers [22–25]. A minor discrepancy in peak locations between the hybrid $Ti_3C_2T_x@ZIF-8$ and the original ZIF-8 might be attributable to

inadequate drying, leaving extra guest molecules and organic linkers that interact with its structure. The disturbed structures were further confirmed in FTIR analysis, which revealed new bonds developing during the in-situ production of a hybrid $\text{Ti}_3\text{C}_2\text{T}_x@\text{ZIF}-8$ catalyst, interfering with crystalline development. However, the pristine $\text{Ti}_3\text{C}_2\text{T}_x$ showed its sharp peak at 7.07° as a successful synthesis of MXene from its MAX phase [26–28]. Based on the comparative analysis, it can be inferred that the incorporation of guest elements into MXene nanosheets has induced significant changes in the molecular framework structure. Additionally, to discern the optimal MXene, X-ray diffraction (XRD) analysis was conducted on multiple samples synthesized at various time intervals, facilitating a more precise selection of the desired MXene. The corresponding XRD results of such MXenes (with varied times) can be seen in Figure S1.

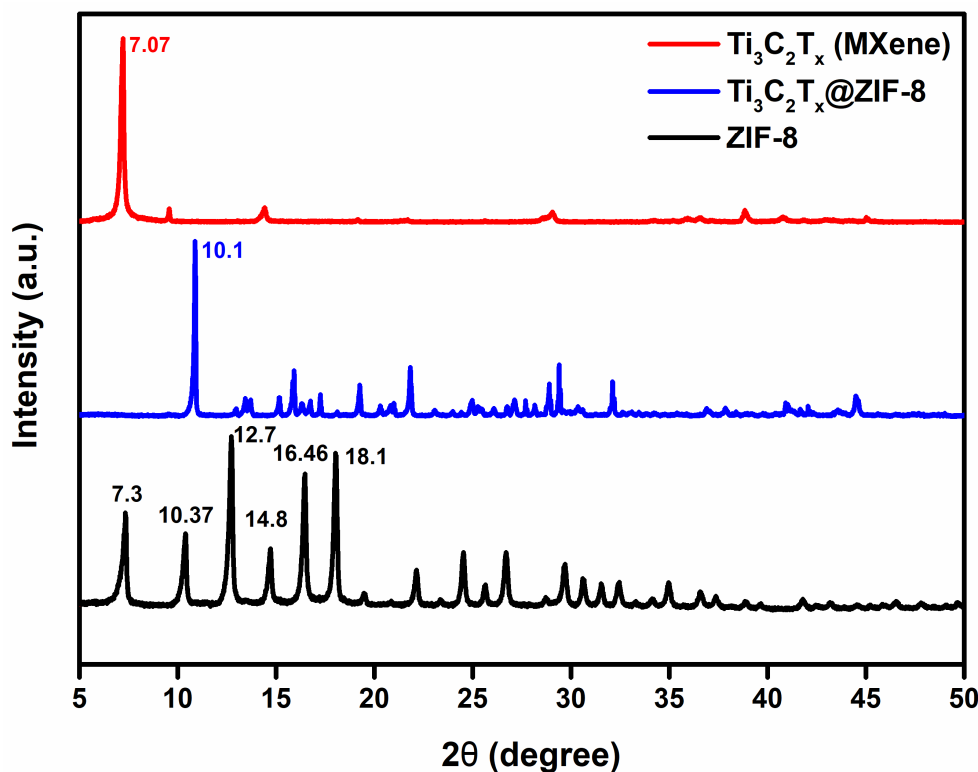


Figure 1. XRD spectra of $\text{Ti}_3\text{C}_2\text{T}_x$, ZIF-8, and $\text{Ti}_3\text{C}_2\text{T}_x@\text{ZIF}-8$.

As-prepared MXene ($\text{Ti}_3\text{C}_2\text{T}_x$) has shown a layered structure (Figure 2a), which can be compared to previous studies related to $\text{Ti}_3\text{C}_2\text{T}_x$ [29,30]. On the other hand, the SEM image of ZIF-8 typically shows a highly textured surface with distinct crystal faces and a characteristic round ball-like shape [31]. The image may also reveal the presence of smaller particles or aggregates, indicating the formation of ZIF-8 nanoparticles, as depicted in Figure 2b [32]. However, combining both elements ($\text{Ti}_3\text{C}_2\text{T}_x$ and ZIF-8) has revealed a mixed morphology. It can be observed through Figure 2c that the image consists of sheet-like (layered) structures along with some spherical existence (ZIF-8), respectively [33]. The mapping of various electrocatalytic materials has been depicted in Figure S2. Through various images from SEM analysis, it was observed that $\text{Ti}_3\text{C}_2\text{T}_x@\text{ZIF}-8$ has a combined morphological characteristic which further assures the successful combination of both elements in terms of surface features toward the desired electrochemical application.

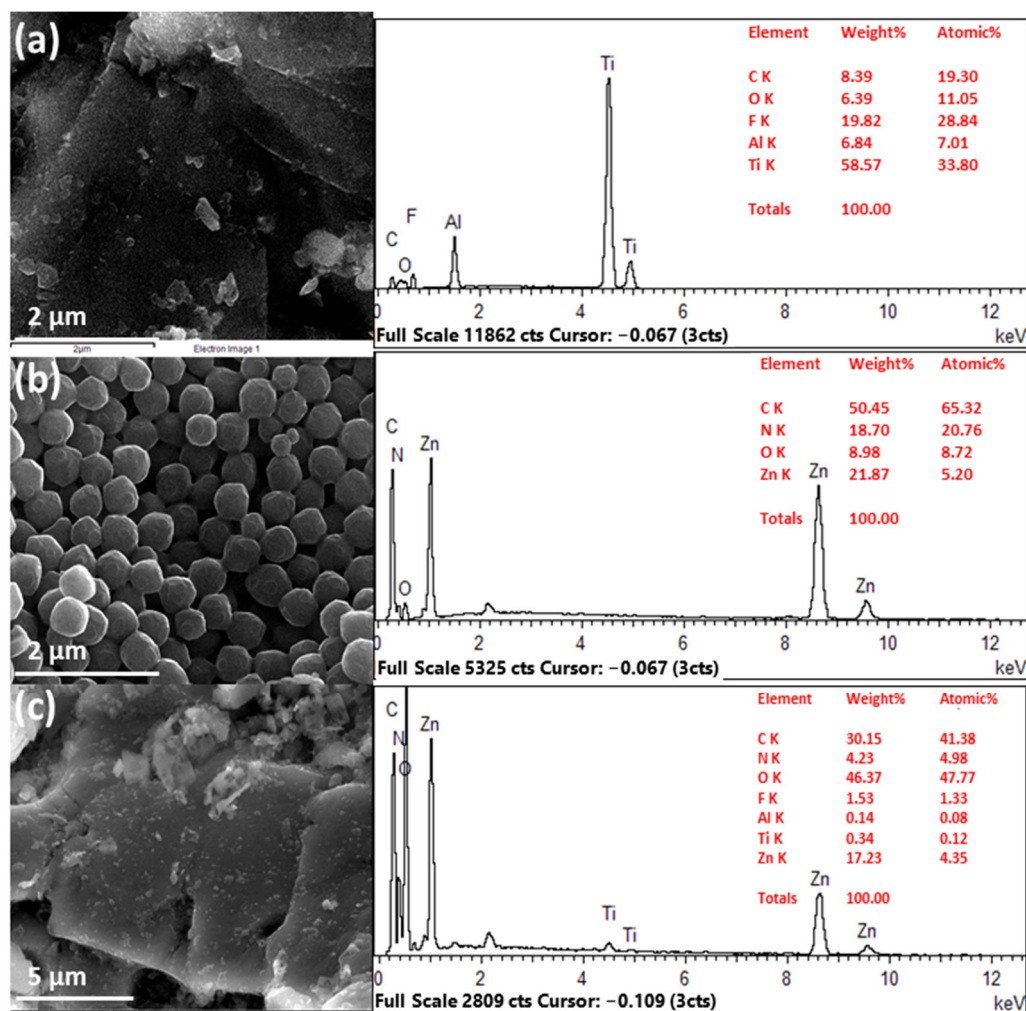


Figure 2. SEM and EDS patterns: (a) $\text{Ti}_3\text{C}_2\text{T}_x$, (b) ZIF-8, and (c) $\text{Ti}_3\text{C}_2\text{T}_x@\text{ZIF-8}$.

FTIR analysis has been carried out for the chemical compound study, as shown in Figure 3. A peak signifying the existence of a Ti-O bond was identified in the $\text{Ti}_3\text{C}_2\text{T}_x$ (MXene) spectra between 400 and 700 cm^{-1} . This may be explained by exposing $\text{Ti}_3\text{C}_2\text{T}_x$ to an oxygen-containing environment, resulting in the oxidation of TiC layers. The vibrations of imidazole units were visible in the mid-infrared region of the FTIR spectrum of pure ZIF-8 ($\text{C}_{24}\text{H}_{30}\text{N}_{12}\text{Zn}_3$). Zn-N vibrations were also discovered in the infrared range of 421 cm^{-1} . Furthermore, C=N stretching was discovered at 1584 cm^{-1} , indicating the FTIR spectrum's resonance with the literature [22,34]. When the FTIR spectra of pure ZIF-8 and hybrid $\text{Ti}_3\text{C}_2\text{T}_x@\text{ZIF-8}$ catalysts were compared, certain peaks formed at the $\text{Ti}_3\text{C}_2\text{T}_x@\text{ZIF-8}$ material, suggesting the creation of bonds during in situ production of ZIF in MXene suspension. It has been proposed that new bonding within hybrid $\text{Ti}_3\text{C}_2\text{T}_x@\text{ZIF-8}$ materials is undesirable because it disrupts the crystalline structure and causes unstable electron fluxes inside the crystalline structure. Although the actual effect of new bonds developing inside hybrid $\text{Ti}_3\text{C}_2\text{T}_x@\text{ZIF-8}$ is yet to be proven, it is still undesirable in terms of adding extra complexity and uncertainty to the electrochemical as well as thermal stability studies.

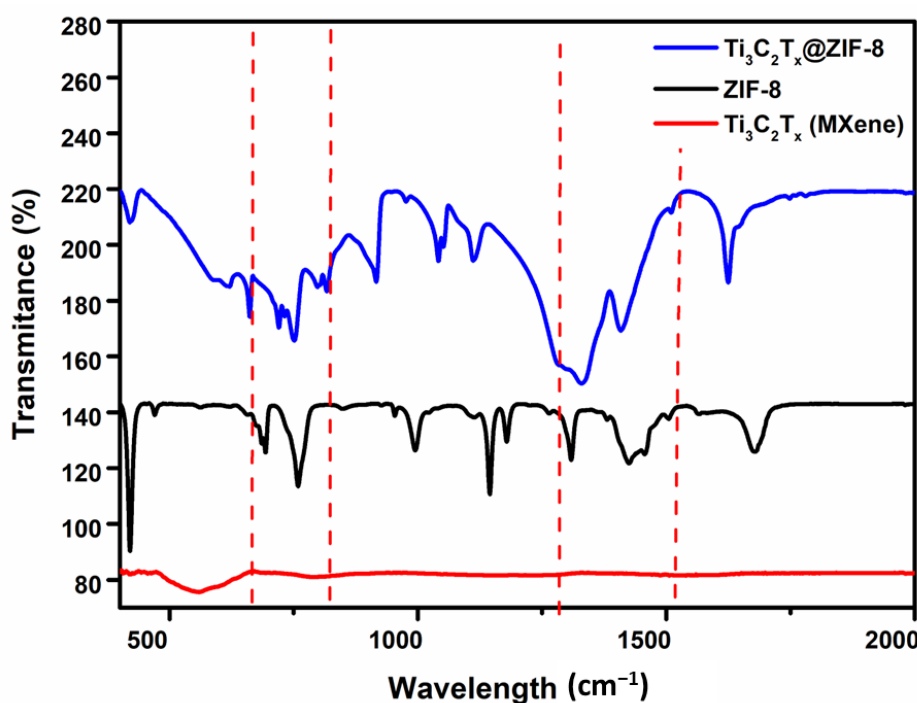


Figure 3. FTIR spectra of $\text{Ti}_3\text{C}_2\text{T}_x$, ZIF-8, and $\text{Ti}_3\text{C}_2\text{T}_x@\text{ZIF-8}$.

High-resolution transmission electron microscopy (HRTEM) was employed to conduct a detailed analysis of the morphology of various materials, as illustrated in Figure 4. Notably, the layered morphology of pristine MXene was observed with a d-spacing value of 0.25 nm, as depicted in Figure 4a [35,36]. The MXene's structure, as well as d-spacing values, have recently been reported. Moreover, the ZIF-8 has demonstrated different circle-shaped particles (Figure 4b). ZIF-8 has a d-spacing value of 0.240 nm [37], which can be seen on the right of Figure 4b. In contrast to MXene as well as ZIF-8's morphological aspects, the combination of both elements ($\text{Ti}_3\text{C}_2\text{T}_x@\text{ZIF-8}$) has combined structures of layers and particles, as depicted in Figure 4c. The $\text{Ti}_3\text{C}_2\text{T}_x@\text{ZIF-8}$ contains the d-spacing value of 0.20 nm [38]. However, the d-spacing value being lower than its pristine materials proves the internal structural changes within the crystal lattice, as previously confirmed through XRD analysis [39,40]. This phenomenon has created internal forces within the ZIF-8 by adding MXene, reducing the inter-planer distance accordingly. The successful combination of ZIF-8 with MXenes has been proven by the HRTEM studies with d-spacing values.

TGA was used to test the thermal stability of synthesized samples by measuring weight loss at heating temperatures ranging from 30 °C to 600 °C in an inert nitrogen atmosphere, as illustrated in Figure 5. A TGA curve will typically show at least three weight changes. The first stage is related to removing strongly bonded water, followed by the breakdown of additional functional groups for materials such as MXene, which has a rich surface functional group composition. Finally, the structural breakdown will be ascribed to the third stage [41].

The minimal quantity of weight losses during the beginning phase was attributed to water evaporation in all samples. $\text{Ti}_3\text{C}_2\text{T}_x$ was shown to have the highest thermal stability among all by exhibiting a nearly straight horizontal curve throughout the TGA measurement, indicating little mass loss of the sample at increased temperatures of up to 600 °C. However, at 526.23 °C and beyond its original mass, a modest increase in the material weight % was recorded. This was caused by the readily oxidized character of $\text{Ti}_3\text{C}_2\text{T}_x$ at the surface. The reaction of Ti and other functional groups in $\text{Ti}_3\text{C}_2\text{T}_x$ with nitrogen or trace amounts of oxygen is more likely to occur at high temperatures. This results in a reduction of F on the surface of MXene and its replacement by O, leading to the creation of TiOF_2 or TiO_2 and a modest increase in total mass. These findings are consistent with the

results of a thermal stability investigation conducted by Hu et al. According to their report, the total weight of MXene Ti_3C_2 increased when the temperature exceeded 400 °C, which was attributed to the production of TiO_2 . Additionally, the investigation also confirmed the creation of oxides by observing a more intense TiO_2 peak with a higher temperature treatment [42]. The initial thermal breakdown of the framework began at 103.23 °C, with a 24.55 wt.% mass loss until it reached 253.35 °C, indicating the carbonization of the ZIF-8 structure, as stated in the equation above [22]. ZIF-8 structural disintegration might be attributed to the expansion of its convoluted bands as well as modifications in its complete ring stretching, in-plane-bending, as well as plane-bending of the imidazole ring. The disintegration of the ZIF-8 structures from 103 °C onwards was caused by the breaking of the Zn-N bonding, the C=N bond, but also the aromatic C-H bonds of the imidazole ring, leading to spectral intensity widening. The results of this study indicate that the thermal stability of ZIF-8 is satisfactory, although not as stable as previously claimed [24,43]. The thermal stability of ZIF-8 was investigated in the temperature range of 253.35 °C to 600 °C. The results indicated that ZIF-8 experienced a mass loss of only 11.48 wt.% during the aforementioned temperature range, which is consistent with previously reported data, indicating a resonant outcome [24]. On the contrary, $\text{Ti}_3\text{C}_2\text{T}_x@\text{ZIF-8}$ exhibited instability, as evidenced by the continuous mass loss observed throughout the spectrum and the absence of a stable phase. This phenomenon may be attributed to the formation of new bonds during the in-situ fabrication process of $\text{Ti}_3\text{C}_2\text{T}_x@\text{ZIF-8}$, which is likely to decrease the material's heat stability as the MXene dose increases.

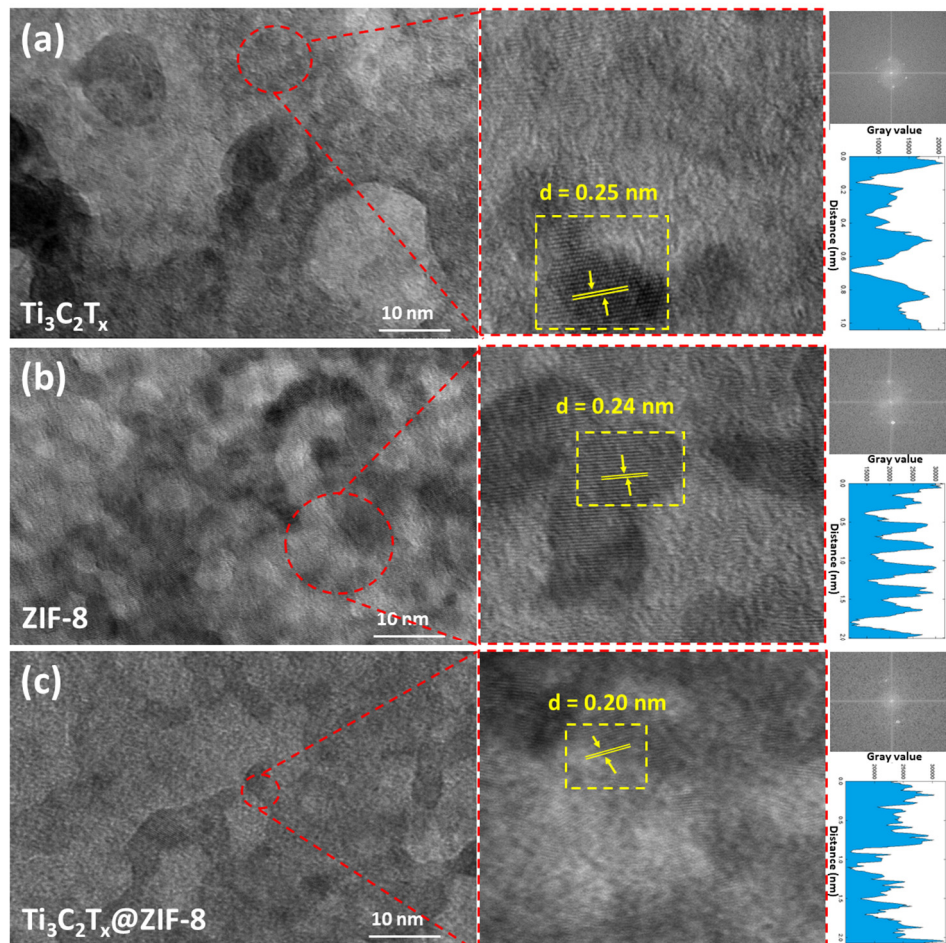


Figure 4. High-resolution transmission electron microscopy (HRTEM) images of various materials, along with their FFT, toward lattice fringes' calculations (on the right): (a) $\text{Ti}_3\text{C}_2\text{T}_x$, (b) ZIF-8, and (c) $\text{Ti}_3\text{C}_2\text{T}_x@\text{ZIF-8}$.

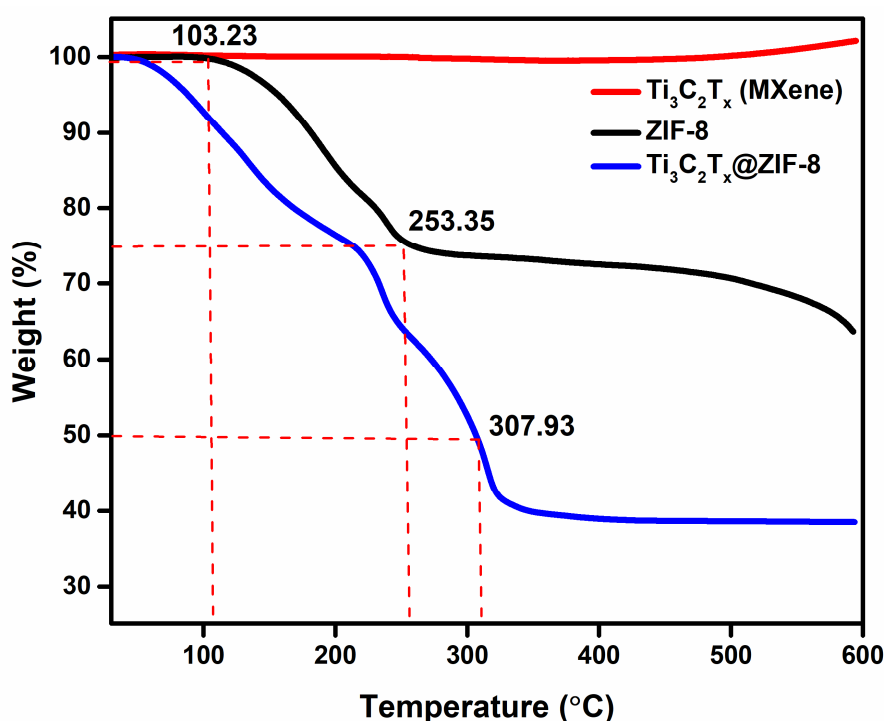
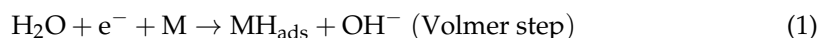


Figure 5. TGA curves of $\text{Ti}_3\text{C}_2\text{T}_x$, ZIF-8, and $\text{Ti}_3\text{C}_2\text{T}_x@\text{ZIF-8}$.

2.2. Electrochemical Response toward HER

Under alkaline circumstances, the HER kinetics are characterized by three stages, as shown in Equations (1)–(3):



The first step is related to the Volmer step, which involves the adsorption of protons onto the electrode surface, as shown in Equation (1), followed by the recombination of adsorbed intermediates, as shown in Equation (2), or the Heyrovsky step, which involves the sorption of the adsorbed species, as shown in Equation (3) [44,45].

Initially, LSV was carried out for the HER response for various electrocatalytic materials, including $\text{Ti}_3\text{C}_2\text{T}_x$, ZIF-8, and the $\text{Ti}_3\text{C}_2\text{T}_x@\text{ZIF-8}$ composite material, as shown in Figure 6a. The figure shows that the onset potential of $\text{Ti}_3\text{C}_2\text{T}_x$ and ZIF is very high, with an overpotential value of 532 and 600 mV. The as-synthesized $\text{Ti}_3\text{C}_2\text{T}_x@\text{ZIF-8}$ material has exhibited a noteworthy shift in onset and overpotential values, measuring at 507 and 20 mA/cm² current densities, respectively. Although its performance falls short of precious metal electrocatalysts such as Pt and Ir, the innovative combination of MXene and ZIF-8 presents a promising new option for HER catalysis. The Nernst equation was used to report the Ag-AgCl reference potential into reversible hydrogen electrode (RHE) potential, as given by Equation (4):

$$E_{\text{RHE}} = E_{\text{Ag}/\text{AgCl}} + 0.059 \text{ pH} + E_{\text{Ag}/\text{AgCl}}^\circ \quad (4)$$

where $E_{\text{Ag}/\text{AgCl}}^\circ$ is 0.2412, and overpotential (η) is calculated by subtracting the onset thermodynamic potential of 0 V for the water-splitting system using Equation (5) [46,47].

$$\text{Overpotential } (\eta) = \text{Onset potential } (E_{\text{RHE}}) \text{ V} - 0 \text{ V} \quad (5)$$

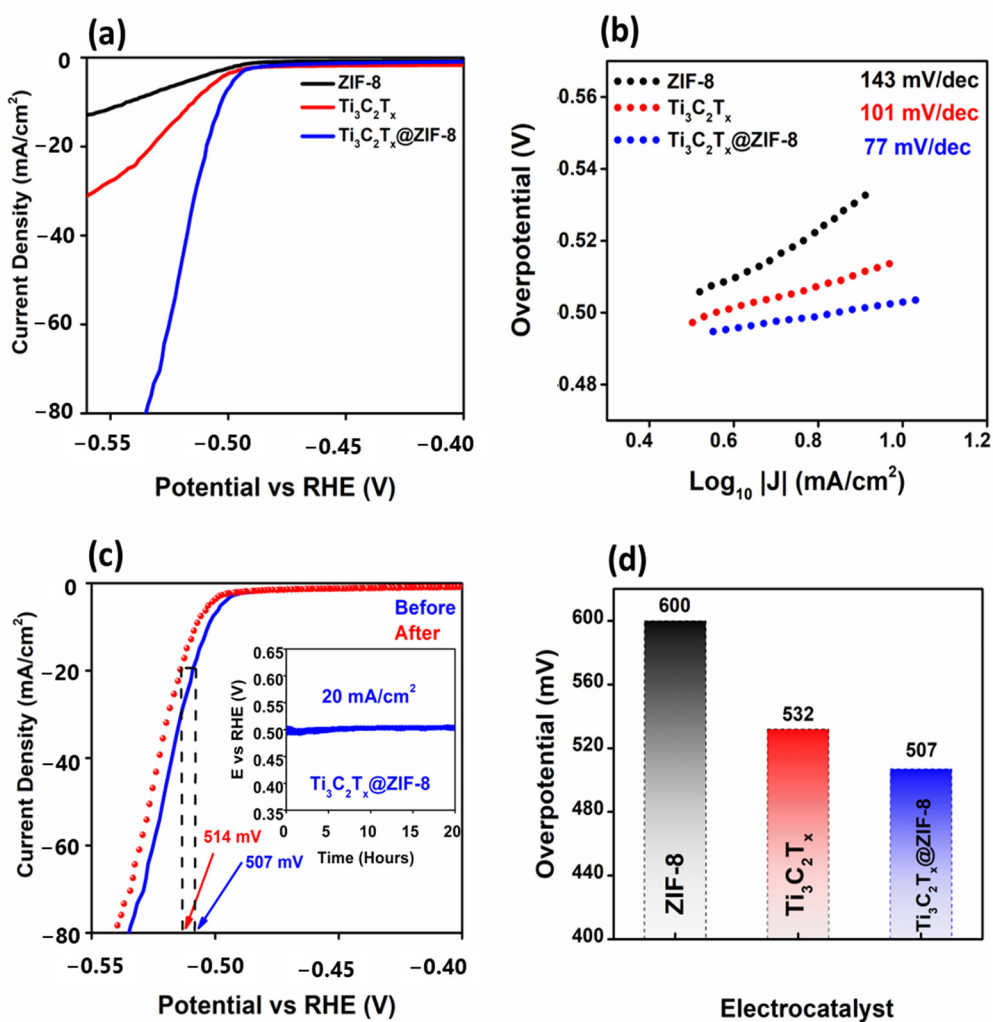


Figure 6. (a) LSV analysis of ZIF-8, Ti₃C₂T_x, and Ti₃C₂T_x@ZIF-8 for the HER response. (b) Tafel slope values (calculated from polarization curves). (c) Stability as well as durability of the Ti₃C₂T_x@ZIF-8 electrocatalyst. (d) Histogram for corresponding overpotential values.

Figure 6b displays the Tafel slope values for electrochemical water splitting, where it acts as the rate-determining step for reaction kinetics, particularly in HER and OER, as indicated by previous studies [48,49]. Higher Tafel slope values of 101 and 143 mV/dec were observed for pristine Ti₃C₂T_x and ZIF-8, respectively, which are significantly greater than the value of 77 mV/dec for the Ti₃C₂T_x@ZIF-8-based electrocatalyst. Therefore, the Ti₃C₂T_x@ZIF-8 electrocatalyst exhibited a faster reaction rate compared to the pristine Ti₃C₂T_x and ZIF-8 materials, as evidenced by its lower Tafel slope value [50]. The corresponding Tafel slope values were obtained using Equation (6):

$$\eta = b \log j + a \quad (6)$$

where η is the overpotential, b is the Tafel slope, and j is the current density.

Furthermore, for the practical application of electrocatalysts, it is essential to thoroughly evaluate their durability and stability towards the HER [51]. Therefore, in order to enhance the electrochemical performance of the synthesized material, a chronopotentiometry test was conducted at a current density of 20 mA/cm². The results of this experiment are presented in Figure 6c. Moreover, Figure 6c shows the durability of the material, which was assessed using linear sweep voltammetry (LSV) before and after the chronopotentiometry test. The polarization curve of the as-prepared material remained almost unchanged with respect to the overpotential and current density, indicating a stable nature of the material.

with minimal changes in overpotential values. These results suggest that the composition ($\text{Ti}_3\text{C}_2\text{T}_x@\text{ZIF}-8$) can further improve electrochemical water-splitting applications. Figure 6d compares the overpotential values of various materials.

To gain a better understanding of the increased HER response of $\text{Ti}_3\text{C}_2\text{T}_x$, ZIF-8, and $\text{Ti}_3\text{C}_2\text{T}_x@\text{ZIF}-8$, the electrochemically active surface area (ECSA) and double-layer capacitance were calculated from the non-faradic region of cyclic voltammetry (CV) curves obtained at various sweep rates (30, 50, and 70 mV/s), as shown in Figure S3a–c. The capacitance values (C_{dl}) were determined by linearly fitting the current density with the scan rate, as illustrated in Figure S3d. The C_{dl} values were found to be 2.8, 1.6, and $4.9 \mu\text{F}/\text{cm}^2$ for $\text{Ti}_3\text{C}_2\text{T}_x$, ZIF-8, and $\text{Ti}_3\text{C}_2\text{T}_x@\text{ZIF}-8$, respectively. The ECSA was derived using C_{dl} values using Equation (7):

$$\text{ECSA} = \frac{C_{dl}}{C_s} \quad (7)$$

where C_{dl} denotes the double-layer capacitance, while C_s denotes the specific capacitance at the electrode interface ($C_s = 0.04 \mu\text{F}/\text{cm}^2$) for the KOH medium, the corresponding ECSA values are presented in Table 1. Nyquist plots were used to analyze the EIS data, and the relevant Nyquist plots are shown in Figure S3e. Table 1 shows the required values from the EIS computation. The composite material ($\text{Ti}_3\text{C}_2\text{T}_x@\text{ZIF}-8$) has demonstrated a superior phase angle compared to $\text{Ti}_3\text{C}_2\text{T}_x$ and ZIF-8. The charge transfer resistance (R_{ct}) values were 1013, 615, and 117 Ω for ZIF-8, $\text{Ti}_3\text{C}_2\text{T}_x$, and $\text{Ti}_3\text{C}_2\text{T}_x@\text{ZIF}-8$, respectively. The low charge transfer resistance of $\text{Ti}_3\text{C}_2\text{T}_x@\text{ZIF}-8$ again verified an excellent charge transfer between the modified electrode and the electrolyte. Hence, accelerated HER kinetics has been demonstrated on the surface of the $\text{Ti}_3\text{C}_2\text{T}_x@\text{ZIF}-8$ composite.

Table 1. Corresponding electrochemical features of various electrocatalytic materials.

Catalyst	Calculation by LSV		Calculation by EIS		Calculation by CV	
	Tafel Slope	Charge Transfer Resistance	Double-Layer Capacitance	Double-Layer Capacitance	Electrochemical Active Surface Area	
	B	R_{ct}	CPE _{dl}	C_{dl}		
	mV/dec	Ω	mF	($\mu\text{F}/\text{cm}^2$)	cm^2	
ZIF-8	143	1013	0.52	1.6	40	
$\text{Ti}_3\text{C}_2\text{T}_x$	101	615	0.71	2.8	70	
$\text{Ti}_3\text{C}_2\text{T}_x@\text{ZIF}-8$	77	117	0.93	4.9	122.5	

3. Experimental Work

3.1. Research Materials

Titanium aluminum carbide (Ti_3AlC_2), 6 M hydrochloric acid (HCl), 2.5 M lithium fluoride (HF), zinc nitrate hexahydrate ($\text{Zn}(\text{NO}_3)_2(6\text{H}_2\text{O})$), 2-methylimidazole ($\text{C}_4\text{H}_6\text{N}_2$), and Nafion were obtained from Sigma-Aldrich Co., Ltd., St. Louis, MO, USA. These materials were all of analytical grade and have been used without further purification.

3.2. Preparation of Desired Electrocatalyst

Titanium carbide ($\text{Ti}_3\text{C}_2\text{T}_x$) MXene was synthesized by removing the metallic “A” layer from Ti_3AlC_2 MAX phase using an etching solution. To prepare the exfoliation etchant, 10 mL of strong HCl (10 M) was diluted with distilled water to form a 6 M solution. Next, 0.648 g of LiF (2.5 M) was added to the HCl (6 M) and stirred for 30 min until completely dissolved. Subsequently, 0.5 g of Ti_3AlC_2 was gradually added to the etchant solution to prevent a violent exothermic reaction [21,52]. The mixture was then stirred on a heated stirrer plate at 40 °C and 260 rpm for 20 min. Next, the well-mixed solution was subjected to microwave irradiation at 40 °C for 10 min, with a ramping time of 27 min, before being cooled to room temperature. The solution was then washed using deionized water with a centrifuge at 8000 rpm for 5 min until it reached a neutral pH of 7. The solution

was then subjected to ultrasonic treatment in an argon environment for 30 min, and the $\text{Ti}_3\text{C}_2\text{T}_x$ supernatant was retrieved and freeze-dried for over 24 h [53]. The above steps were repeated with varying microwave irradiation periods of 15, 20, 25, 30, 35, and 40 min while keeping the other parameters (temperature, ramping time) constant.

To create the precursor solution, a mixture of 1.20 g of zinc nitrate hexahydrate and 16 g of 2-methyl imidazole was completely dissolved in 20 mL of methanol. The solution was centrifuged at 1000 rpm for 5 min to separate the ZIF particles from the solution. Subsequently, the resulting solution was purified with methanol and dried overnight in a vacuum oven at 40 °C [34,54].

To create $\text{Ti}_3\text{C}_2\text{T}_x$ encapsulated in ZIF-8, 2.95 mg of $\text{Ti}_3\text{C}_2\text{T}_x$ nanoparticles were sonicated for 1 h in 36 mL of methanol with zinc hexahydrate (1.2 g). This constructed hybrid catalyst was left to dry overnight at 60 °C under vacuum after 2-methylimidazole (2.6 g) was dissolved in the sonicated mixture by stirring at 35 °C for 4 h [23]. The same steps were repeated for $\text{Ti}_3\text{C}_2\text{T}_x$ wt.% of 0.5%, 1%, 1.5%, and 2% to investigate the optimum MXene amount to be added. However, we have chosen 1.5% and marked as $\text{Ti}_3\text{C}_2\text{T}_x@\text{ZIF-8}$ (as per electrochemical results).

3.3. Electrochemical Analysis

Pure $\text{Ti}_3\text{C}_2\text{T}_x$, ZIF-8, and $\text{Ti}_3\text{C}_2\text{T}_x@\text{ZIF-8}$ nanostructure materials were subjected to different electrochemical tests for HER performance in an alkaline environment using a 1.0 M KOH solution. The tests were conducted using a potentiostat, Ametek VersaSTAT4 (Pittsburgh, PA, USA), with a prepared silver silver-chloride (Ag/AgCl) as a reference electrode, a platinum (Pt) wire as a counter-electrode, and a glassy carbon electrode (GCE) as the working electrode. Each catalyst material (10 mg) was dispersed in 2 mL of deionized water with 0.5 mL of a 5% Nafion solution (as a binder). Then, 30 μL of each catalyst solution was deposited on GCE and dried at room temperature using an electric air blower. The HER analysis was performed using LSV, with a potential range of 0 V to −1.6 V at a scan range of 5 mV/s. EIS was used with a sinusoidal potential of 5 mV and an onset HER potential at frequency ranges from 100 kHz to 0.1 Hz. CV was performed to calculate the double-layer capacitance (C_{dl}) at applied potential ranges from 0.05 V to 0.25 V at different scan rates (30, 50, and 70 mV/s). For a stable electrochemical performance, chronopotentiometry was performed on the $\text{Ti}_3\text{C}_2\text{T}_x@\text{ZIF-8}$ composite for 20 h, and durability was checked before and after the stability test on the same device.

3.4. Material Characterizations

Crystallographic studies were conducted using X-ray diffraction (XRD) by examining powder X-ray diffraction patterns in 2θ range of 5 to 90° (step size = 0.01°) using CuK radiation (=1.5418 Å) on a Rigaku SmartLab powder X-ray diffractometer (Rigaku, Tokyo, Japan). The surface morphology and microstructure of the prepared materials were characterized using a scanning electron microscope (SEM), FEI Quanta 400 (FEI Company, Hillsboro, OR, USA) equipped with energy dispersive X-ray spectroscopy (EDS), Oxford-Instruments INCA 400 (Oxford-Instruments, Abingdon, UK) with X-Max Detector. A transmission electron microscope (TEM), FEI Tecnai G2 F20 (FEI Company, Hillsboro, OR, USA), equipped with EDS, Oxford X-MaxN 80T (Oxford-Instruments, Abingdon, UK), was used to record the material's morphology and elemental distribution. The chemical bonding of the electrocatalytic materials was examined using PerkinElmer, Spectrum Two FT-IR spectrometer (PerkinElmer, Waltham, MA, USA) at the scan range between 200 and 3000 cm^{-1} with 4 cm^{-1} resolution. The sample's thermal stability was determined using thermogravimetric analysis (TGA) by analyzing the link between the steadily increasing temperature and the catalyst weight remaining in the furnace. TGA studies were conducted in the temperature range of 25–600 °C at a rate of 10 °C/min under nitrogen gas flow conditions using a PerkinElmer thermogravimetric analyzer, STA 6000 (PerkinElmer, Waltham, MA, USA).

4. Conclusions

The as-prepared material ($\text{Ti}_3\text{C}_2\text{T}_x@\text{ZIF}-8$) was prepared through different synthesis processes. $\text{Ti}_3\text{C}_2\text{T}_x@\text{ZIF}-8$ was characterized through various tests, including SEM, XRD, HRTEM, XPS, and FTIR, for morphology, crystallinity, chemical composition, and bonding, respectively. It was observed that the $\text{Ti}_3\text{C}_2\text{T}_x$ MXenes had a variety of sheet-like 2D structures which resembled the MXene's morphology, and the addition of ZIF-8 contributed to a change in the morphology as well as the crystallinity of the material to introduce impurity within the structure. The $\text{Ti}_3\text{C}_2\text{T}_x@\text{ZIF}-8$ composite demonstrated faster reaction kinetics for HER, having an overpotential value of 507 mV, along with a Tafel slope value of 77 mV/dec and electrochemical stability for 20 h at 20 mA/cm² through the chronopotentiometry test. However, the $\text{Ti}_3\text{C}_2\text{T}_x@\text{ZIF}-8$ still requires further study to enhance its desired properties to compete with precious metal-based electrocatalysts. Meanwhile, such electrochemical aspects and the stable nature of the electrocatalytic material under alkaline media support its remarkable applicability in energy storage and conversion systems toward a sustainable future.

Supplementary Materials: The following supporting information can be downloaded at: <https://www.mdpi.com/article/10.3390/catal13050802/s1>, Figure S1: XRD of MXene $\text{Ti}_3\text{C}_2\text{T}_x$ with microwave irradiation time of 15–40 min. Figure S2: EDS elemental mapping of various materials (a) $\text{Ti}_3\text{C}_2\text{T}_x$ (b) ZIF-8 (c) $\text{Ti}_3\text{C}_2\text{T}_x@\text{ZIF}-8$. Figure S3: CV curves of various materials at scan rates of 30, 50, and 70 mV/s; (a) $\text{Ti}_3\text{C}_2\text{T}_x$ (b) ZIF-8 (c) $\text{Ti}_3\text{C}_2\text{T}_x@\text{ZIF}-8$. (d) Double layer capacitance (CdL) values which are calculated from CV scan rates by linear fitting of potential as well as current densities (e) Nyquist plots (calculated through EIS analysis) for various materials.

Author Contributions: Conceptualization, M.K., R.W. and W.Y.W.; methodology, M.K., R.W. and A.H.; formal analysis, L.P.H., A.H. and W.Y.W.; investigation, L.P.H., A.H. and F.B.; resources, R.W., M.K. and C.P.; data curation, L.P.H., A.H. and F.B.; writing—original draft preparation, L.P.H. and A.H.; writing—review and editing, M.K., R.W. and W.Y.W.; supervision, M.K., R.W. and C.P.; project administration, M.K. and R.W.; funding acquisition, M.K. and C.P. All authors have read and agreed to the published version of the manuscript.

Funding: The authors thank the support of Xiamen University Malaysia and Sunway University for research funding through Rewarding Research Output (GRTIN-RRO-48-2022) and the International Research Network Grant Scheme, 2022 (STR-IRNGS-SET-GAMRG-01-2021).

Data Availability Statement: The data are included as Supplementary Materials and in the article.

Conflicts of Interest: The authors declare no conflict of interest.

References

1. Barelli, L.; Bidini, G.; Gallorini, F.; Servili, S. Hydrogen production through sorption-enhanced steam methane reforming and membrane technology: A review. *Energy* **2008**, *33*, 554–570. [[CrossRef](#)]
2. Zou, X.; Zhang, Y. Noble metal-free hydrogen evolution catalysts for water splitting. *Chem. Soc. Rev.* **2015**, *44*, 5148–5180. [[CrossRef](#)] [[PubMed](#)]
3. Chandrasekaran, S.; Khandelwal, M.; Dayong, F.; Sui, L.; Chung, J.S.; Misra, R.D.K.; Yin, P.; Kim, E.J.; Kim, W.; Vanchiappan, A.; et al. Developments and Perspectives on Robust Nano- and Microstructured Binder-Free Electrodes for Bifunctional Water Electrolysis and Beyond. *Adv. Energy Mater.* **2022**, *12*, 2200409. [[CrossRef](#)]
4. Yin, J.; Wei, K.; Bai, Y.; Liu, Y.; Zhang, Q.; Wang, J.; Qin, Z.; Jiao, T. Integration of amorphous CoSnO_3 onto wrinkled MXene nanosheets as efficient electrocatalysts for alkaline hydrogen evolution. *Sep. Purif. Technol.* **2023**, *308*, 122947. [[CrossRef](#)]
5. Hanan, A.; Solangi, M.Y.; Jaleel Laghari, A.; Shah, A.A.; Aftab, U.; Ibupoto, Z.A.; Abro, M.I.; Lakhani, M.N.; Soomro, I.A.; Dawi, E.A.; et al. $\text{PdO}@\text{CoSe}_2$ composites: Efficient electrocatalysts for water oxidation in alkaline media. *RSC Adv.* **2022**, *13*, 743–755. [[CrossRef](#)]
6. Devendra, B.K.; Praveen, B.M.; Tripathi, V.S.; Nagaraju, D.H.; Nayana, K.O. Hydrogen Evolution Reaction by Platinum Coating. *Iran. J. Sci. Technol. Trans. A Sci.* **2021**, *45*, 1993–2000. [[CrossRef](#)]
7. Yang, F.; Chen, Y.; Cheng, G.; Chen, S.; Luo, W. Ultrathin nitrogen-doped carbon coated with CoP for efficient hydrogen evolution. *ACS Catal.* **2017**, *7*, 3824–3831. [[CrossRef](#)]
8. Aftab, U.; Tahira, A.; Samo, A.H.; Abro, M.I.; Baloch, M.M.; Kumar, M.; Sirajuddin; Ibupoto, Z.H. Mixed $\text{CoS}_2@\text{Co}_3\text{O}_4$ composite material: An efficient nonprecious electrocatalyst for hydrogen evolution reaction. *Int. J. Hydrogen Energy* **2020**, *45*, 13805–13813. [[CrossRef](#)]

9. Yin, J.; Zhan, F.; Jiao, T.; Wang, W.; Zhang, G.; Jiao, J.; Jiang, G.; Zhang, Q.; Gu, J.; Peng, Q. Facile preparation of self-assembled MXene@Au@CdS nanocomposite with enhanced photocatalytic hydrogen production activity. *Sci. China Mater.* **2020**, *63*, 2228–2238. [[CrossRef](#)]
10. Abdelghafar, F.; Xu, X.; Jiang, S.P.; Shao, Z. Designing single-atom catalysts toward improved alkaline hydrogen evolution reaction. *Mater. Rep. Energy* **2022**, *2*, 100144. [[CrossRef](#)]
11. Xu, X.; Shao, Z.; Jiang, S.P. High-Entropy Materials for Water Electrolysis. *Energy Technol.* **2022**, *10*, 2200573. [[CrossRef](#)]
12. Tang, J.; Xu, X.; Tang, T.; Zhong, Y.; Shao, Z. Perovskite-Based Electrocatalysts for Cost-Effective Ultrahigh-Current-Density Water Splitting in Anion Exchange Membrane Electrolyzer Cell. *Small Methods* **2022**, *6*, 2201099. [[CrossRef](#)] [[PubMed](#)]
13. Wen, X.; Guan, J. Recent progress on MOF-derived electrocatalysts for hydrogen evolution reaction. *Appl. Mater. Today* **2019**, *16*, 146–168. [[CrossRef](#)]
14. Yin, J.; Zhan, F.; Jiao, T.; Deng, H.; Zou, G.; Bai, Z.; Zhang, Q.; Peng, Q. Highly efficient catalytic performances of nitro compounds via hierarchical PdNPs-loaded MXene/polymer nanocomposites synthesized through electrospinning strategy for wastewater treatment. *Chin. Chem. Lett.* **2020**, *31*, 992–995. [[CrossRef](#)]
15. Peralta, D.; Chaplais, G.; Simon-Masseron, A.; Barthelet, K.; Pirngruber, G.D. Synthesis and adsorption properties of ZIF-76 isomorphs. *Microporous Mesoporous Mater.* **2012**, *153*, 1–7. [[CrossRef](#)]
16. Naguib, M.; Kurtoglu, M.; Presser, V.; Lu, J.; Niu, J.; Heon, M.; Hultman, L.; Gogotsi, Y.; Barsoum, M.W. Two-dimensional nanocrystals produced by exfoliation of Ti₃AlC₂. *Adv. Mater.* **2011**, *23*, 4248–4253. [[CrossRef](#)] [[PubMed](#)]
17. Zheng, Z.; Guo, C.; Wang, E.; He, Z.; Liang, T.; Yang, T.; Hou, X. The oxidation and thermal stability of two-dimensional transition metal carbides and/or carbonitrides (MXenes) and the improvement based on their surface state. *Inorg. Chem. Front.* **2021**, *8*, 2164–2182. [[CrossRef](#)]
18. Li, X.; Huang, Z.; Shuck, C.E.; Liang, G.; Gogotsi, Y.; Zhi, C. MXene chemistry, electrochemistry and energy storage applications. *Nat. Rev. Chem.* **2022**, *6*, 389–404. [[CrossRef](#)]
19. Peng, J.; Chen, X.; Ong, W.-J.; Zhao, X.; Li, N. Surface and heterointerface engineering of 2D MXenes and their nanocomposites: Insights into electro-and photocatalysis. *Chem* **2019**, *5*, 18–50. [[CrossRef](#)]
20. Wu, H.; Almalki, M.; Xu, X.; Lei, Y.; Ming, F.; Mallick, A.; Roddatis, V.; Lopatin, S.; Shekhah, O.; Eddaoudi, M.; et al. MXene Derived Metal–Organic Frameworks. *J. Am. Chem. Soc.* **2019**, *141*, 20037–20042. [[CrossRef](#)]
21. Zong, H.; Qi, R.; Yu, K.; Zhu, Z. Ultrathin Ti₂NT_x MXene-wrapped MOF-derived CoP frameworks towards hydrogen evolution and water oxidation. *Electrochim. Acta* **2021**, *393*, 139068. [[CrossRef](#)]
22. James, J.B.; Lin, Y. Kinetics of ZIF-8 thermal decomposition in inert, oxidizing, and reducing environments. *J. Phys. Chem. C* **2016**, *120*, 14015–14026. [[CrossRef](#)]
23. Radwan, A.; Jin, H.; Liu, B.; Chen, Z.; Wu, Q.; Zhao, X.; He, D.; Mu, S. 3D-ZIF scaffold derived carbon encapsulated iron nitride as a synergistic catalyst for ORR and zinc-air battery cathodes. *Carbon* **2021**, *171*, 368–375. [[CrossRef](#)]
24. Yin, H.; Kim, H.; Choi, J.; Yip, A.C. Thermal stability of ZIF-8 under oxidative and inert environments: A practical perspective on using ZIF-8 as a catalyst support. *Chem. Eng. J.* **2015**, *278*, 293–300. [[CrossRef](#)]
25. Md Nordin, N.A.H.; Ismail, A.F.; Yahya, N. Zeolitic imidazole framework 8 decorated graphene oxide (ZIF-8/GO) mixed matrix membrane (mmm) for CO₂/CH₄ separation. *J. Teknol.* **2017**, *79*. [[CrossRef](#)]
26. Wang, B.X.; Shu, Q.; Chen, H.D.; Xing, X.Y.; Wu, Q.; Zhang, L. Copper-Decorated Ti₃C₂T_x MXene Electrocatalyst for Hydrogen Evolution Reaction. *Metals* **2022**, *12*, 2022. [[CrossRef](#)]
27. Yang, Y.Y.; Yu, Z.L.; An, X.W.; Duan, X.H.; Chen, M.; Zhang, J.; Hao, X.G.; Abudula, A.; Guan, G.Q. Ti₃C₂T_x nanosheets with uniformly anchored Ru nanoparticles for efficient acidic and basic hydrogen evolution reaction. *Int. J. Hydrogen Energy* **2023**, *48*, 9163–9171. [[CrossRef](#)]
28. Zhang, P.; Fan, C.C.; Wang, R.R.; Xu, C.X.; Cheng, J.G.; Wang, L.C.; Lu, Y.W.; Luo, P.F. Pd/MXene(Ti₃C₂T_x)/reduced graphene oxide hybrid catalyst for methanol electrooxidation. *Nanotechnology* **2020**, *31*, 09LT01. [[CrossRef](#)]
29. Cui, G.; Wang, L.; Li, L.; Xie, W.; Gu, G. Synthesis of CuS nanoparticles decorated Ti₃C₂T_x MXene with enhanced microwave absorption performance. *Prog. Nat. Sci. Mater. Int.* **2020**, *30*, 343–351. [[CrossRef](#)]
30. Nagarajan, R.D.; Sundaramurthy, A.; Sundramoorthy, A.K. Synthesis and characterization of MXene (Ti₃C₂T_x)/Iron oxide composite for ultrasensitive electrochemical detection of hydrogen peroxide. *Chemosphere* **2022**, *286*, 131478. [[CrossRef](#)]
31. Abdollahi, B.; Najafidoust, A.; Abbasi Asl, E.; Sillanpaa, M. Fabrication of ZIF-8 metal organic framework (MOFs)-based CuO-ZnO photocatalyst with enhanced solar-light-driven property for degradation of organic dyes. *Arab. J. Chem.* **2021**, *14*, 103444. [[CrossRef](#)]
32. Ni, W.; Xiao, X.; Geng, W.; Zhang, L.; Li, Y.; Li, N. Controllable preparation of amino-functionalized ZIF-8: A functionalized MOF material for adsorbing Congo Red and Eriochrome Black T in aqueous solution. *JCIS Open* **2021**, *3*, 100018. [[CrossRef](#)]
33. Choi, E.; Lee, J.; Kim, Y.-J.; Kim, H.; Kim, M.; Hong, J.; Kang, Y.C.; Koo, C.M.; Kim, D.W.; Kim, S.J. Enhanced stability of Ti₃C₂T_x MXene enabled by continuous ZIF-8 coating. *Carbon* **2022**, *191*, 593–599. [[CrossRef](#)]
34. Butova, V.V.; Budnik, A.P.; Bulanova, E.A.; Soldatov, A.V. New microwave-assisted synthesis of ZIF-8. *Mendeleev Commun.* **2016**, *1*, 43–44. [[CrossRef](#)]
35. Luo, J.; Matios, E.; Wang, H.; Tao, X.; Li, W. Interfacial structure design of MXene-based nanomaterials for electrochemical energy storage and conversion. *Informat* **2020**, *2*, 1057–1076. [[CrossRef](#)]

36. Zhao, G.; Lv, H.; Zhou, Y.; Zheng, X.; Wu, C.; Xu, C. Self-Assembled Sandwich-like MXene-Derived Nanocomposites for Enhanced Electromagnetic Wave Absorption. *ACS Appl. Mater. Interfaces* **2018**, *10*, 42925–42932. [[CrossRef](#)]
37. Ravinayagam, V.; Rehman, S. Zeolitic imidazolate framework-8 (ZIF-8) doped TiZSM-5 and Mesoporous carbon for antibacterial characterization. *Saudi J. Biol. Sci.* **2020**, *27*, 1726–1736. [[CrossRef](#)]
38. Zhao, N.; Zhang, F.; Zhan, F.; Yi, D.; Yang, Y.; Cui, W.; Wang, X. Fe³⁺-stabilized Ti₃C₂T_x MXene enables ultrastable Li-ion storage at low temperature. *J. Mater. Sci. Technol.* **2021**, *67*, 156–164. [[CrossRef](#)]
39. Luo, J.; Zhang, W.; Yuan, H.; Jin, C.; Zhang, L.; Huang, H.; Liang, C.; Xia, Y.; Zhang, J.; Gan, Y.; et al. Pillared Structure Design of MXene with Ultralarge Interlayer Spacing for High-Performance Lithium-Ion Capacitors. *ACS Nano* **2017**, *11*, 2459–2469. [[CrossRef](#)]
40. Guo, X.; He, S.; Meng, Z.; Wang, Y.; Peng, Y. Ag@ZIF-8/g-C₃N₄ Z-scheme photocatalyst for the enhanced removal of multiple classes of antibiotics by integrated adsorption and photocatalytic degradation under visible light irradiation. *RSC Adv.* **2022**, *12*, 17919–17931. [[CrossRef](#)]
41. Liu, R.; Li, W. High-thermal-stability and high-thermal-conductivity Ti₃C₂T_x MXene/poly (vinyl alcohol)(PVA) composites. *ACS Omega* **2018**, *3*, 2609–2617. [[CrossRef](#)] [[PubMed](#)]
42. Hu, S.; Li, S.; Xu, W.; Zhang, J.; Zhou, Y.; Cheng, Z. Rapid preparation, thermal stability and electromagnetic interference shielding properties of two-dimensional Ti₃C₂ MXene. *Ceram. Int.* **2019**, *45*, 19902–19909. [[CrossRef](#)]
43. Liu, Y.; Cheng, H.; Cheng, M.; Liu, Z.; Huang, D.; Zhang, G.; Shao, B.; Liang, Q.; Luo, S.; Wu, T. The application of Zeolitic imidazolate frameworks (ZIFs) and their derivatives based materials for photocatalytic hydrogen evolution and pollutants treatment. *Chem. Eng. J.* **2021**, *417*, 127914. [[CrossRef](#)]
44. QayoomMugheri, A.; AneelaTahira; Aftab, U.; IshaqAbro, M.; Chaudhry, S.R.; Amaral, L.; Ibupoto, Z.H. Co₃O₄/NiO bifunctional electrocatalyst for water splitting. *Electrochim. Acta* **2019**, *306*, 9–17. [[CrossRef](#)]
45. Hanan, A.; Lakhan, M.N.; Shu, D.; Hussain, A.; Ahmed, M.; Soomro, I.A.; Kumar, V.; Cao, D. An efficient and durable bifunctional electrocatalyst based on PdO and Co₂FeO₄ for HER and OER. *Int. J. Hydrogen Energy* **2023**. [[CrossRef](#)]
46. Hanan, A.; Shu, D.; Aftab, U.; Cao, D.; Laghari, A.J.; Solangi, M.Y.; Abro, M.I.; Nafady, A.; Vigolo, B.; Tahira, A.; et al. Co₂FeO₄@rGO composite: Towards trifunctional water splitting in alkaline media. *Int. J. Hydrogen Energy* **2022**, *47*, 33919–33937. [[CrossRef](#)]
47. Ahmed, M.; Lakhan, M.N.; Shar, A.H.; Zehra, I.; Hanan, A.; Ali, I.; Latif, M.A.; Chand, K.; Ali, A.; Wang, J. Electrochemical performance of grown layer of Ni(OH)₂ on nickel foam and treatment with phosphide and selenide for efficient water splitting. *J. Indian Chem. Soc.* **2022**, *99*, 100281. [[CrossRef](#)]
48. Hanan, A.; Ahmed, M.; Lakhan, M.N.; Shar, A.H.; Cao, D.; Asif, A.; Ali, A.; Gul, M. Novel rGO@Fe₃O₄ nanostructures: An active electrocatalyst for hydrogen evolution reaction in alkaline media. *J. Indian Chem. Soc.* **2022**, *99*, 100442. [[CrossRef](#)]
49. Samo, A.; Aftab, U.; Cao, D.; Ahmed, M.; Lakhan, M.; Kumar, V.; Asif, A.; Ali, A. Schematic synthesis of cobalt-oxide (Co₃O₄) supported cobalt-sulfide (CoS) composite for oxygen evolution reaction. *Dig. J. Nanomat. Biostructures* **2022**, *17*, 109–120. [[CrossRef](#)]
50. Laghari, A.J.; Aftab, U.; Tahira, A.; Shah, A.A.; Gradone, A.; Solangi, M.Y.; Samo, A.H.; Kumar, M.; Abro, M.I.; Akhtar, M.w.; et al. MgO as promoter for electrocatalytic activities of Co₃O₄–MgO composite via abundant oxygen vacancies and Co²⁺ ions towards oxygen evolution reaction. *Int. J. Hydrogen Energy* **2023**, *48*, 12672–12682. [[CrossRef](#)]
51. Huo, D.K.; Sun, Z.C.; Liu, Y.Y.; Yu, Z.Q.; Wang, Y.; Wang, A.J. Synthesis of Co-Doped Tungsten Phosphide Nanoparticles Supported on Carbon Supports as High-Efficiency HER Catalysts. *Acs Sustain. Chem. Eng.* **2021**, *9*, 12311–12322. [[CrossRef](#)]
52. Zhang, T.; Pan, L.; Tang, H.; Du, F.; Guo, Y.; Qiu, T.; Yang, J. Synthesis of two-dimensional Ti₃C₂T_x MXene using HCl+ LiF etchant: Enhanced exfoliation and delamination. *J. Alloys Compd.* **2017**, *695*, 818–826. [[CrossRef](#)]
53. Xia, Y.; Mathis, T.S.; Zhao, M.-Q.; Anasori, B.; Dang, A.; Zhou, Z.; Cho, H.; Gogotsi, Y.; Yang, S. Thickness-independent capacitance of vertically aligned liquid-crystalline MXenes. *Nature* **2018**, *557*, 409–412. [[CrossRef](#)] [[PubMed](#)]
54. Lai, L.S.; Yeong, Y.F.; Lau, K.K.; Shariff, A.M. Effect of synthesis parameters on the formation of ZIF-8 under microwave-assisted solvothermal. *Procedia Eng.* **2016**, *148*, 35–42. [[CrossRef](#)]

Disclaimer/Publisher's Note: The statements, opinions and data contained in all publications are solely those of the individual author(s) and contributor(s) and not of MDPI and/or the editor(s). MDPI and/or the editor(s) disclaim responsibility for any injury to people or property resulting from any ideas, methods, instructions or products referred to in the content.